

Cite this: *CrystEngComm*, 2011, **13**, 2123

www.rsc.org/crystengcomm

PAPER

# Porous Co<sub>3</sub>O<sub>4</sub> microcubes: hydrothermal synthesis, catalytic and magnetic properties

Feng Cao,<sup>ab</sup> Deqiang Wang,<sup>ab</sup> Ruiping Deng,<sup>ab</sup> Jinkui Tang,<sup>ab</sup> Shuyan Song,<sup>ab</sup> Yongqian Lei,<sup>ab</sup> Song Wang,<sup>ab</sup> Shengqun Su,<sup>ab</sup> Xiangguang Yang<sup>ab</sup> and Hongjie Zhang<sup>\*ab</sup>

Received 10th July 2010, Accepted 24th November 2010

DOI: 10.1039/c0ce00392a

Well-defined porous Co<sub>3</sub>O<sub>4</sub> microcubes have been synthesized by a simple one-pot solvothermal method combined with subsequent calcination. The formation mechanism of the cube-like precursor was proposed based on the anisotropic intrinsic structure of CoCO<sub>3</sub>. Importantly, after thermal treatment, the cube-like morphology could be completely preserved. Moreover, the thermal decomposition of the corresponding precursor led to the formation of porous structure. The effects of calcination temperature on the catalytic properties of Co<sub>3</sub>O<sub>4</sub> samples were investigated and the results demonstrated that 600 °C was superior among three samples with the highest catalytic properties. Additionally, as an antiferromagnetic material, the sample showed a certain degree of ferromagnetism under the external magnetic field.

## Introduction

Controlling the shape, size, and structure of inorganic nano-materials have been attracting researchers' intensive attention because of the expectation of novel properties.<sup>1</sup> Currently, the synthesis of mesoporous materials has been the focus of much attention due to their potential applications in catalysis, sensors, fuel cells, supercapacitors and so on.<sup>2</sup> However, it is still a big challenge to develop simple and reliable synthetic methods for porous architectures with designed chemical components and controlled morphologies, which strongly affect the properties of nanomaterials.

Cobalt oxide is one of the most promising functional materials due to its wide range of application in catalytic reaction, lithium-ion batteries, gas sensors, and supercapacitors.<sup>3</sup> For example, Co<sub>3</sub>O<sub>4</sub> nanowires and nano-needles have been recently demonstrated as an improved negative electrode for lithium-ion batteries.<sup>4</sup> Additionally, Co<sub>3</sub>O<sub>4</sub> nanocrystalline have been used as a catalyst for selective alkane oxidation under ambient conditions and exhibit exceptional properties for the oxidation of some short chain alkanes.<sup>5</sup> Due to these important properties, well-defined Co<sub>3</sub>O<sub>4</sub> nanostructures with various morphologies including nanowires,<sup>6</sup> nanorods,<sup>7</sup> nanocubes,<sup>8</sup> nanospheres,<sup>9</sup> nanoflowers<sup>10</sup> and nanosheets<sup>11</sup> have been synthesized successfully using a variety of methods, such as direct elemental reaction at high temperature,<sup>12</sup> epoxide synthetic route,<sup>13</sup> microwave-

assisted reflux method,<sup>14</sup> inverse micro-emulsion,<sup>15</sup> solvothermal and hydrothermal methods<sup>16</sup> with the aim of expanding its application scope. The impetus of our research here is to synthesize novel nanostructures and study their excellent properties.

In this paper, uniform cube-like cobalt carbonate crystals have been synthesized in high yield *via* a simple solvothermal method. Furthermore, the effects of reaction parameters on the formation of nanostructures and their formation mechanism were also discussed. Mesoporous microcubes of spinel Co<sub>3</sub>O<sub>4</sub> were synthesized by the thermal treatment of the corresponding CoCO<sub>3</sub> precursor in air at high temperatures. The catalytic properties of these mesoporous microcubes were found to be influenced greatly by varying the calcination temperatures. To the best of our knowledge, the effects of calcination temperature on the catalytic properties of Co<sub>3</sub>O<sub>4</sub> samples have not yet been systematically investigated.

## Experimental

### Preparation of samples

All chemicals used in this experiment were of analytical grade and used as received. In a typical synthesis, 0.5 mmol of Co(NO<sub>3</sub>)<sub>2</sub>·4H<sub>2</sub>O was dissolved and stirred in a mixed solvent of 18 mL of diethylene glycol (DEG) and 2 mL of H<sub>2</sub>O. 1 g CO(NH<sub>2</sub>)<sub>2</sub> was added after the Co(NO<sub>3</sub>)<sub>2</sub>·4H<sub>2</sub>O was completely dissolved. After 10 min of stirring, the resulting reaction mixture was transferred into a 25 mL Teflon-lined autoclave. Finally, the autoclave was sealed and maintained at 180 °C for 24 h and then cooled down to room temperature naturally. The precipitate was separated by centrifugation, washed with distilled water and absolute ethanol several times, and dried at 60 °C for 2 h.

<sup>a</sup>State Key Laboratory of Rare Earth Resource Utilization Chinese Academy of Sciences, Changchun Institute of Applied Chemistry, P. R. China. E-mail: hongjie@ciac.jl.cn; Fax: +86-431-85698041; Tel: +86-431-85262127

<sup>b</sup>Graduate School of the Chinese Academy of Sciences, Beijing, 100039, P. R. China

## Characterization of samples

The X-ray diffraction pattern of the products was performed on a Rigaku-D/max 2500 V X-ray diffractometer with Cu-K $\alpha$  radiation ( $\lambda = 1.5418 \text{ \AA}$ ), with an operation voltage and current maintained at 40 kV and 40 mA. The samples were prepared by sonicating powdered samples in ethanol, then evaporating one drop of the suspension on a glass slide. Field-emission scanning electron microscopy (FESEM) images were obtained with a XL30 ESEM FEG microscope. The samples were prepared by sonicating powdered samples in ethanol, then evaporating one drop of suspension on a Si slide, and then evaporating a thin gold film on the slide. Transmission electron microscopic (TEM) images, high-resolution transmission electron microscopic (HRTEM) images and selected area electron diffraction (SAED) patterns were obtained on a JEOL JEM-2010 microscope.

## Catalytic tests

The liquid-phase oxidation of cyclohexane was adopted to evaluate the redox property of the materials. Typically, 10 g cyclohexane, 100 mg catalysts were added into a 50 mL autoclave reactor with a Teflon bar inside. When the heating jacket reached the temperature 403 K, another forty minute was acquired to make the balance between the reactor and the heating jacket before charging O<sub>2</sub> to 1.0 MPa and stirring. During reaction, oxygen was replenished to 1.0 MPa once the pressure declined to 0.9 MPa, with which we can control the amount of O<sub>2</sub> consumed. When the reaction was stopped, the reaction mixture was diluted with 15 g ethanol to dissolve the by-products. KA oil was quantified by GC equipped with a DM-5 column (530 mm  $\times$  1 mm  $\times$  30 mm) using toluene as the internal standard, and the acid and ester by acid–base titration.

## Magnetic measurement

Magnetic measurements were performed on the powder samples using a Quantum Design MPMS XL-7 SQUID magnetometer equipped with a 7 T magnet.

## Results and discussion

### Precursor characterization

The phase composition and structure of the precursors were first investigated by XRD. All the peaks in XRD pattern in Fig. 1 can be readily indexed to a CoCO<sub>3</sub> phase (JCPDS card no. 11-0692). No characteristic peaks from other crystalline impurities were detected, thus indicating the formation of pure products.

The morphology and size of the as-synthesized products were characterized by FESEM. The low-magnification FESEM image (Fig. 2a) reveals that the product is composed of uniform ordered microcubes in high yield. The high-magnification FESEM image (Fig. 2b) clearly shows that the size of the whole microcube is around 3–4  $\mu\text{m}$ . Interestingly, the microcubes are in fact constructed with two-dimensional nanoplates, while these tiny plates are attached side by side in an ordered fashion. The chemical composition of these microcubes was further determined by EDS (Fig. 2a, inset). Peaks of the elements Co, C and O are detected in the EDS pattern and the molar ratio is about 1 : 1 : 3.

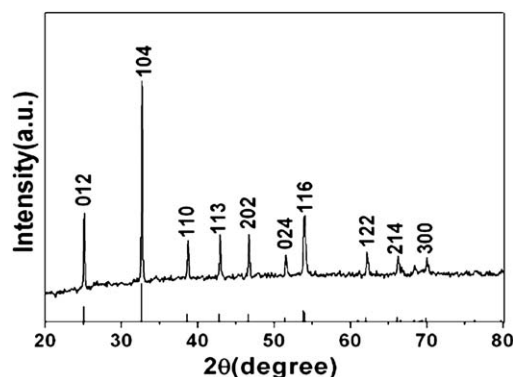


Fig. 1 XRD pattern of the as-prepared precursor.

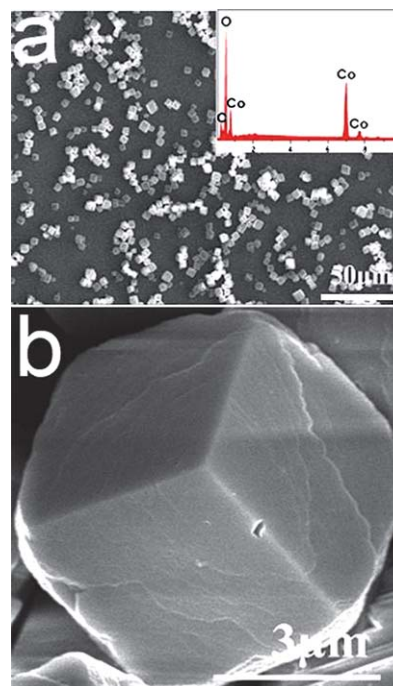


Fig. 2 (a) Low-magnification SEM image of the precursor CoCO<sub>3</sub> microcubes and the EDS pattern (inset). (b) Enlarged SEM image of the CoCO<sub>3</sub> microcubes.

The thermal stability of the precursor was examined by TG-DTA analysis (Fig. 3). The TG curve exhibited that a smooth decomposition occurred at an onset temperature of approximately 280 °C and a completion temperature of approximately 395 °C. Moreover, a total weight loss of 32.52% attributed to the decomposition of carbonate in the precursor, which is in excellent agreement with the calculation of 32.51% mass loss based on that CoCO<sub>3</sub> decomposed to Co<sub>3</sub>O<sub>4</sub>. Above 400 °C there was no weight loss, indicating the complete decomposition of the organic species and formation of pure Co<sub>3</sub>O<sub>4</sub>. As observed in the DTA curve, the first exothermic peak at about 280 °C was associated with absorption water lost and the remnant surfactant decomposition. The prominent exothermic peak at 380 °C is the result of the degradation of CoCO<sub>3</sub>. The final exothermic peak at about 532 °C can be attributed to the crystallization of the Co<sub>3</sub>O<sub>4</sub> phase, basically agreeing with the result of XRD.

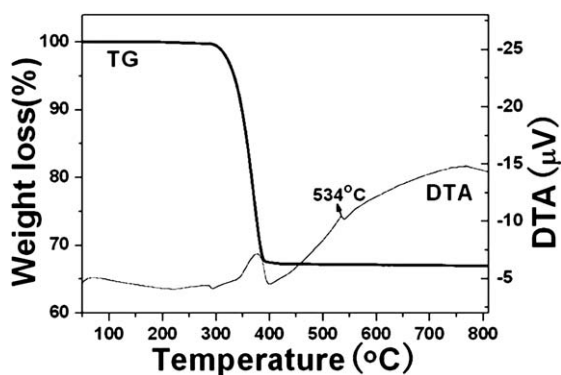


Fig. 3 TG and DTA curves of the precursor.

### Influences of reaction parameters on the shape of the precursors

The morphologies and crystal phase purity of the as-prepared microcrystal are mainly affected by the following experimental conditions, such as reaction time, the addition of DEG and  $\text{CO}(\text{NH}_2)_2$ , and the ratio of  $\text{H}_2\text{O}$  to DEG, which has been discussed in detail as follows. Firstly, we systematically studied the effect of the volume ratio of  $\text{H}_2\text{O}$  and DEG on the structure and morphology of the resultant product. When different volume ratios of  $\text{H}_2\text{O}/\text{DEG}$  were used in the reaction system, the corresponding sizes and morphology variations of  $\text{CoCO}_3$  product were shown in Fig. 4. As can be seen in Fig. 4a, without the addition of DEG,  $\text{CoCO}_3$  crystals tend to grow into an irregular polyhedral structure with a wide distribution range from 20 to 30  $\mu\text{m}$ . The size of  $\text{CoCO}_3$  microcubes decreased as the amount of DEG increased. It is clear that the amount of DEG plays an

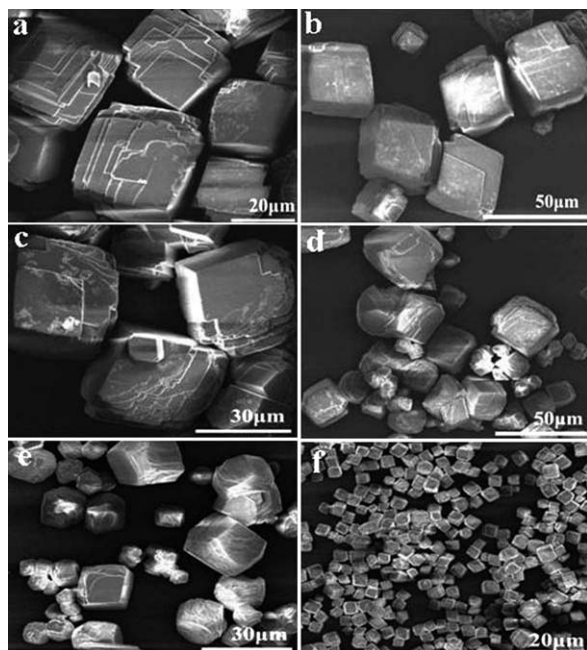


Fig. 4 SEM images of the samples prepared under different  $\text{H}_2\text{O}/\text{DEG}$  volume ratios: (a) pure  $\text{H}_2\text{O}$ , (b) 3 : 2, (c) 1 : 1, (d) 9 : 1, (e) 4 : 1, (f) pure DEG. In all cases, samples were prepared at 200  $^{\circ}\text{C}$ , and a reaction time of 24 h.

important role for the sizes and shapes of the resulted microcubes. A plausible explanation to this phenomenon could be due to the increase of viscosity in the reaction system, which might cause the diffusion of ions or growing unit more difficult and suppress the anisotropic growth of  $\text{CoCO}_3$  nanoparticles.<sup>17</sup> We know that DEG is a complexing agent with a relatively high boiling point and viscosity, and has been widely used in the polyol process to provide monodisperse fine metal or metal oxide nanoparticles.<sup>18</sup>

Secondly, it is worthwhile to mention that the addition of urea has strong effects on the formation of the well-defined cube-like nanostructures. Fig. 5 shows FESEM images of the samples obtained when different amounts of urea (from 0–2 g) are introduced into the reaction system. Without using urea, microflowers with diameters of about 1  $\mu\text{m}$  are the dominant products in the batch solution (Fig. 5a). When 0.05 g of urea is added, some polyhedron-like structures emerge from the products, although the dominant product remains irregular microflowers (Fig. 5b). Further increasing the amount of urea (0.1 g), more and more polyhedrons appear in the product together with a decreased amount of flower-like structures (Fig. 5c). When the

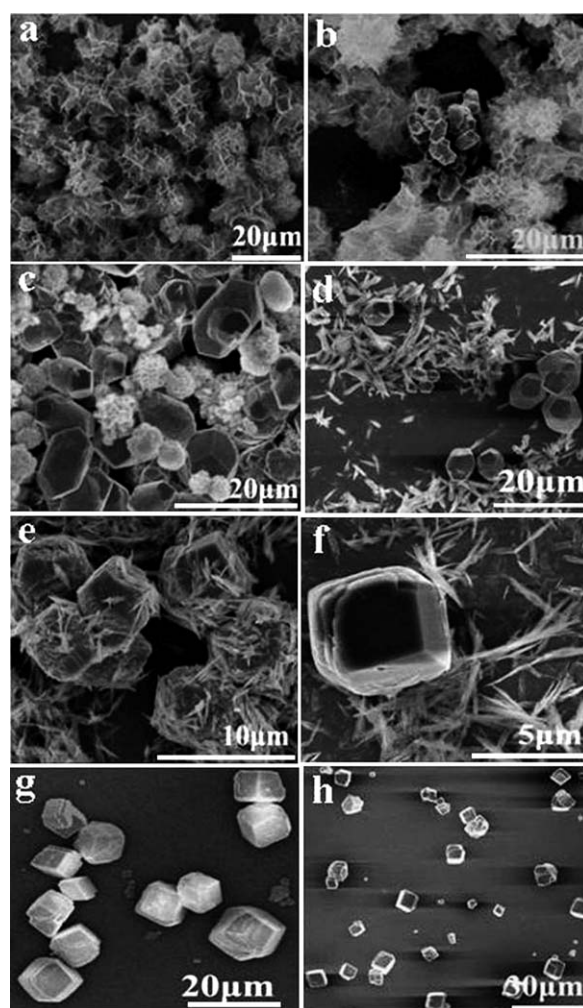


Fig. 5 SEM images of the samples with different amounts of urea keeping the other conditions unchanged: (a) 0 g, (b) 0.05 g, (c) 0.1 g, (d) 0.15 g, (e) 0.2 g, (f) 0.5 g, (g) 0.6 g, (h) 2 g.



addition of urea is up to 0.15 g, there are also two morphologies coexisting in the system, namely, interlaced packed platelets and irregular polyhedrons (Fig. 5d). More interestingly, in this stage, flower-like morphologies disappeared and packed platelet-like morphologies appeared instead. When the quantity of urea is further increased (0.2 to 0.5 g), the packed platelet-like structures and quasicube-shaped products coexist in the sample, both with uniform sizes (Fig. 5e and f). When increasing the amount of urea amounts to 0.6 g, cube-like architectures are the only morphology (Fig. 5g). When the quantity of urea is further increased (2 g), the morphology still remains cube-like architectures without an obvious change (Fig. 5h). So the addition of urea is to be very critical in this synthesis method.

It has been reported that urea in aqueous solution can be used to provide a steady  $\text{OH}^-$  ion by hydrolysis of  $\text{CO}(\text{NH}_2)_2$ .<sup>19</sup> When no urea was added under the same reaction conditions, the  $[\text{OH}^-]$  in the reaction solution without adding urea is much lower than that of containing  $\text{CO}(\text{NH}_2)_2$ , and thus the production rate of precursor  $\text{CoCO}_3$  is slow. In this case, the collision rate between  $\text{CoCO}_3$  crystals is much quicker than the growth rate of a single  $\text{CoCO}_3$  crystal particle in solution, and then as the reaction proceeds, flower-like agglomerates can be obtained through random aggregation to reduce the surface energy.<sup>20</sup>

In order to understand the formation process of the precursor, time-dependent experiments were performed. Fig. 6 shows the SEM images of the samples obtained at different time intervals. When the reaction time was 1 h, only thin sheet-like morphologies could be formed (Fig. 6a). When the reaction time was extended to 2 h, cube-like products could be clearly observed as shown in Fig. 6b. The image indicated that these cubes formed in the flake aggregates. On further prolonging the reaction time (Fig. 6c), the amount of microcubes increased at the expense of the sheets. Eventually no sheets remained and the sample was composed entirely of the cube-like nanostructure, as shown in Fig. 6d. From this point, the size and morphology of the product remained the same even at longer reaction times.

In this formation process, time was the most important controlling factor. At the beginning of the reaction, when mixing

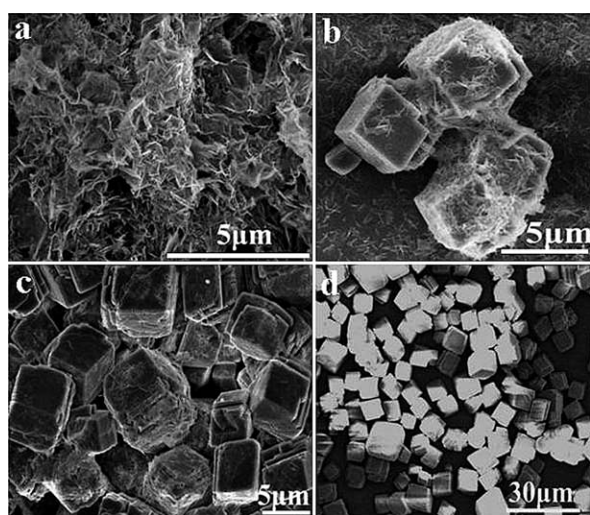


**Fig. 6** SEM images of the products at 180 °C obtained at different times: (a) 1 h, (b) 2 h, (c) 5 h and (d) 8 h.

the DEG and  $\text{Co}(\text{NO}_3)_2$  solution in the basic condition,  $\text{Co}^{2+}$  can interact with DEG molecules to form precursor complexes which decrease the free  $\text{Co}^{2+}$  ion concentration and reduce the rate of crystal growth.<sup>21</sup> Under solvothermal conditions (high temperature and pressure), the complex chelating would be weakened and  $\text{CoCO}_3$  precursor would be released gradually. In the following secondary growth, these precursor nanocrystals grow into nanoplates owing to the intrinsic lamellar structures of these materials. From the structural images of  $\text{CoCO}_3$  (Fig. 7), it can be seen that (100) and (010) facets bear more dangling bonds (which determine the chemical potential based on Gibbs–Thomson law) than any other facets, so the crystal growth along the [100] and [010] directions can release more energy, thus making the (100) and (010) facets of higher chemical potential than the other facets.<sup>22</sup> Therefore,  $\text{CoCO}_3$  crystals were induced to grow to nanosheets under such conditions. Then, these  $\text{CoCO}_3$  primary microcubes were formed through the self-assembly aggregation of the nanosheets at higher solvothermal temperatures, driven by the minimization of interfacial energy. With the increase of reaction time, the primary cubes continue to grow, finally forming the well-defined microcubes. Several forces such as electrostatic and dipolar fields associated with the aggregate, hydrophobic interactions, hydrogen bonds, crystal-face attraction, and van der Waals forces may have various effects on the self-assembly.<sup>23</sup> Further work is under way to investigate the detail of the self-assembly process.

### $\text{Co}_3\text{O}_4$ preparation and characterization

The XRD patterns shown in Fig. 8 correspond to the samples obtained by thermal treatment of the precursor at 400, 600 and 800 °C in air for 2 h. All the reflection peaks could be readily indexed to  $\text{Co}_3\text{O}_4$  (space group  $Fd\bar{3}m$ ) and with a lattice constant  $a = 8.064 \text{ \AA}$ , which agrees well with the reported data (JCPDS 43-1003). No other impurity peaks can be detected, indicating a complete decomposition of the  $\text{CoCO}_3$  precursor into pure  $\text{Co}_3\text{O}_4$  after calcination. Additionally, the degree of crystallinity is observed to increase with increasing the calcination temperature from 400 to 600 °C. However, further increasing the heat treatment temperature to 800 °C induces the reduction of the crystallinity of the  $\text{Co}_3\text{O}_4$  microcube sample. Because a relatively strong sintering is apparently produced for the sample calcined at 800 °C.<sup>24</sup>

Further evidence for the quality and composition was obtained by XPS of the black product, and the XPS spectrum of  $\text{Co}_3\text{O}_4$  was identified. The binding energies obtained in the XPS analysis were corrected for specimen charging, through

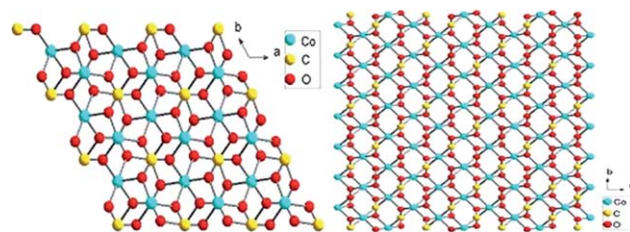


**Fig. 7** Schematic illustration of the precursor  $\text{CoCO}_3$  crystal structure viewed from the  $c$  axis (left) and  $a$  axis (right).

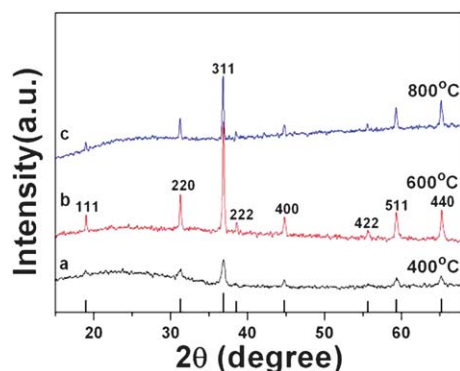


**Fig. 8** XRD patterns of the Co<sub>3</sub>O<sub>4</sub> nanostructures annealed at different temperatures: (a) 400, (b) 600 and (c) 800 °C and the standard card of Co<sub>3</sub>O<sub>4</sub> (JCPDS no. 43-1003) as a reference.

referencing the C 1s to 284.70 eV. As shown in Fig. 9, It seems that all three samples have identical peaks. There are two strong peaks at about 779.8 and 794.8 eV, which can be attributed to Co 2p<sub>3/2</sub> and Co 2p<sub>1/2</sub>, respectively. The peaks at 530.1 eV can be assigned to O 1s. These results are fully consistent with our XRD observations.

The morphology and size of the as-produced cobalt oxide were characterized by FESEM and TEM. As shown in Fig. 10, the overview of Co<sub>3</sub>O<sub>4</sub> exhibits that the cube-like morphology keeps unchanged after calcination ranging from 400 to 800 °C. From the high-magnetization FESEM, we can clearly observe that the porous structure becomes more apparent with increasing calcination temperature. Because heat treatment made CoCO<sub>3</sub> precursor decomposed to Co<sub>3</sub>O<sub>4</sub> completely. During decomposing process, lots of bubbles of CO<sub>2</sub> produced in the reaction provide the porous center and finally porous Co<sub>3</sub>O<sub>4</sub> microcubes

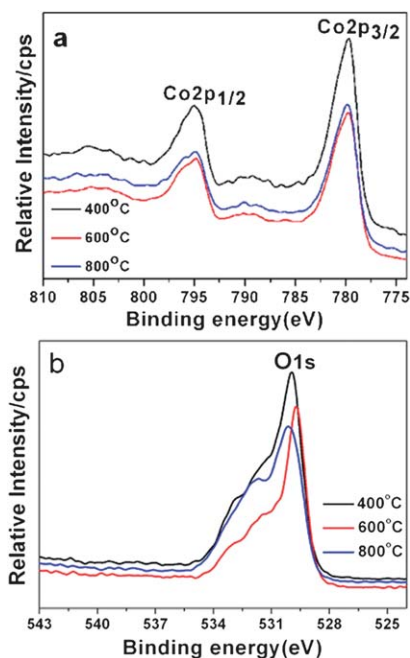


**Fig. 9** XPS analysis for the samples annealed at different temperatures: (a) 400, (b) 600 and (c) 800 °C.

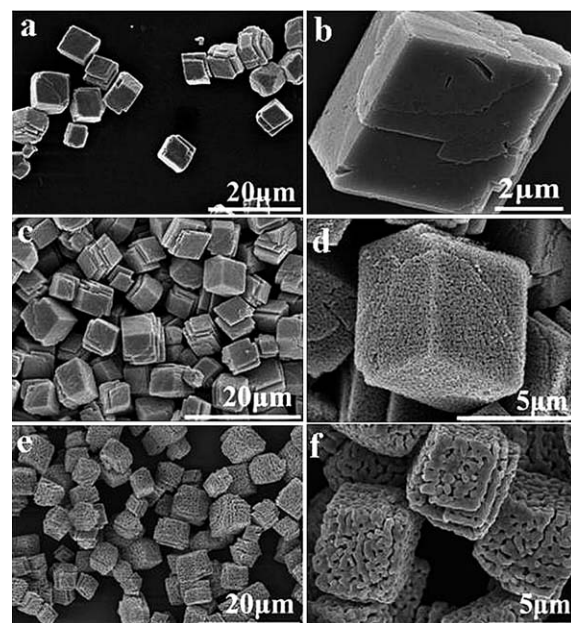


**Fig. 10** SEM images of the as-prepared samples calcined at 400 (a, b), 600 (c, d) and 800 °C (e, f).

were formed.<sup>25</sup> After annealing at high temperatures, the microcube diameters decrease greatly accompanied by the changes on the surface properties due to the decomposition of the organic species and the formation of inorganic phase. Fig. 11a, d and g show the typical TEM images of Co<sub>3</sub>O<sub>4</sub> microcubes. The TEM images were in good agreement with the morphology as presented in the SEM picture. Additionally, it is obvious that the pores of the samples become large greatly with increasing the calcined temperatures. However, the cube architectures of the Co<sub>3</sub>O<sub>4</sub> samples annealed at 800 °C is poorly

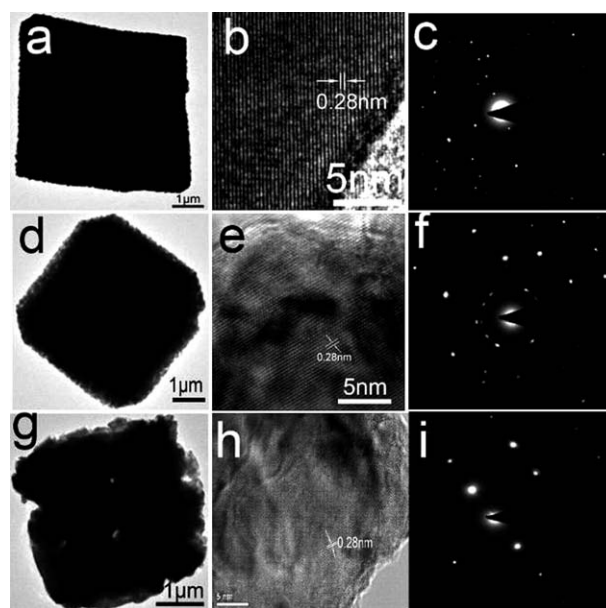


**Fig. 11** TEM, HRTEM and SAED images of the typical samples calcined at 400 (a, b, c), 600 (d, e, f) and 800 °C (g, h, i).

ordered relative to other samples calcined at other temperatures. The size of the cubes was reduced to *ca.* 2  $\mu\text{m}$  due to sinter phenomenon under too high temperature. Further insight into the morphology and microstructure of cube-shaped  $\text{Co}_3\text{O}_4$  nanostructures was gained by using HRTEM and SAED (Fig. 11). The representative HRTEM images of the edge areas of the  $\text{Co}_3\text{O}_4$  microcubes in Fig. 11 exhibit well-resolved 2D lattice fringes, further confirming the single-crystal nature of the microcubes. The plane spacing of 0.28 nm corresponds to the lattice planes of (222) in  $\text{Co}_3\text{O}_4$ . The SAED patterns in Fig. 11 taken from the edges of microcubes reveal highly single crystalline nature of the  $\text{Co}_3\text{O}_4$  microcubes.

### Catalytic performance

In view of the unique redox behaviour, cobalt-containing materials have always been used as effective catalysts in the selective oxidation of cyclohexane.<sup>26</sup> As an important homogeneous catalyst,  $\text{Co}_3\text{O}_4$  nanocrystal has been extensively employed for the cyclohexane oxidation.<sup>27</sup> It is well-known that the sizes, shapes, and structures of the catalyst materials are closely related to the catalytic performance.<sup>28</sup> However, very little is known about the influence of calcination temperature on  $\text{Co}_3\text{O}_4$  nanocrystals' catalytic activity. Herein, we studied the catalytic activity of porous  $\text{Co}_3\text{O}_4$  microcubes calcined at different temperatures. The results were listed in Table 1. We can see that all the three  $\text{Co}_3\text{O}_4$  samples show good reactivity. In detail, sample 2 (calcined at 600  $^\circ\text{C}$ ) achieved a conversion of 7.9% and 81.7% selectivity to KA oil, which is the most efficient catalyst of the three samples. Sample 1 (calcined at 400  $^\circ\text{C}$ ) gave a 25% decrease in conversion compared to the sample 2. Although the conversion of sample 3 is almost the same as sample 1's, there was a 26.9% increase in the yield of by-product. The different reactivity of the three samples shown may be subjected to the crystallization of  $\text{Co}_3\text{O}_4$ , and the sinter phenomenon.<sup>24</sup> The XRD pattern in Fig. 9 shows that the crystallization of sample 1 is obviously imperfect, although there is no weight loss observed in TG-DTA curve of Fig. 3. As for the sample 3, sinter is the main reason for its low selectivity which can be informed from Fig. 11. Therefore, 600  $^\circ\text{C}$  is the optimal calcination temperature for the materials to be catalyst used in cyclohexane oxidation. The studies on calcination temperature-associated catalytic activities of different  $\text{Co}_3\text{O}_4$  microcubes will help us to understand other catalyst nanocrystals and thus offer great opportunities to explore the dependence of a material's properties on the morphology and structure and find many interesting applications in the catalytic field.

**Table 1** Catalytic activity data for oxidation of cyclohexane over the sample calcined at: (1) 400, (2) 600 and (3) 800  $^\circ\text{C}$

Catalyst	Conversion(%)	Distribution of products (%)		
		Cyclohexanol	Cyclohexanone	By-product
1	5.9	39.3	42.3	18.4
2	7.9	41.0	39.7	19.3
3	7.2	32.9	42.6	24.5

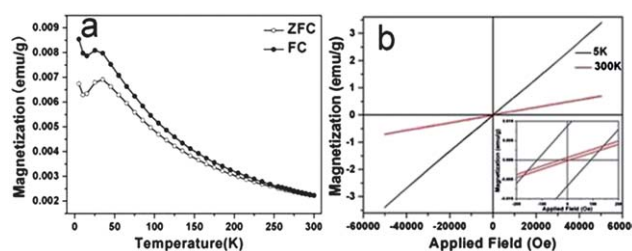


**Fig. 12** (a) Temperature dependence of ZFC and FC magnetization for the microcubes under an applied field of 100 Oe. (b) Magnetic hysteresis curves measured at 5 and 300 K, and the down-right inset are the magnified hysteresis loops at low applied field ( $-200 \text{ Oe} < H < 200 \text{ Oe}$ ).

### Magnetic study

The magnetic properties of the sample calcined at 600  $^\circ\text{C}$  were accessed by recording both the temperature-dependent magnetization and the magnetic hysteresis curves. As shown in Fig. 12a, the magnetization increases with decreasing of temperature to reach a maximum at  $\sim 35 \text{ K}$ , before decreasing to a minimum at 15 K and further lowering of temperature from 15 K to 5 K leads to increase of magnetization. This indicates that  $\text{Co}_3\text{O}_4$  nanomaterial mainly shows antiferromagnetic properties. However, the broad peak at  $\sim 35 \text{ K}$  suggests that nanoporous  $\text{Co}_3\text{O}_4$  nanomaterial has weak ferromagnetic behaviour at low temperature. A similar phenomenon is also found in the  $\text{Co}_3\text{O}_4$  nanowires and nanotubes reported by previous literatures.<sup>29</sup>

To further probe the magnetic properties of the sample, we also measured the magnetic hysteresis loops up to 5 T at 5 and 300 K, respectively. As shown in Fig. 12b, both curves exhibit a little ferromagnetic property, as a little coercive force and remnant magnetization can be seen. As an anti-ferromagnetic material, the  $\text{Co}_3\text{O}_4$  microcube shows a certain degree of ferromagnetism under the external magnetic field. There are two reasons explained for this: the unpaired atom spins orientation near the surface of the nanocrystals and the interaction of atoms.<sup>30</sup>

### Conclusions

In summary, a facile method for generating well-defined  $\text{Co}_3\text{O}_4$  cube-like architectures with porosity has been described. The approach involves thermal decomposition of the precursor  $\text{CoCO}_3$ . The formation mechanism of the cube-like precursor is proposed based on the anisotropic intrinsic structure of  $\text{CoCO}_3$ . Importantly, the thermal decomposition of the corresponding precursor leads to the formation of the mesoporous structure and the cube-like morphology retains unchanged after thermal treatment. The effects of calcination temperature on the catalytic properties of  $\text{Co}_3\text{O}_4$  samples were investigated and the results demonstrate that 600  $^\circ\text{C}$  is superior among three samples with the highest catalytic properties. Additionally, as an anti-ferromagnetic material, the sample show a certain degree of ferromagnetism under the external magnetic field.

### Acknowledgements

The authors are grateful to the financial aid from the National Natural Science Foundation of China (grant no. 20490210,



20631040, 2006BAE03B03-03 and 20610102007) and the MOST of China ('973' Program, grant no. 2006CB601103).

## References

- (a) X. Wang, J. Zhuang, Q. Peng and Y. D. Li, *Nature*, 2005, **437**, 121; (b) J. Zhang, Z. Lin, Y. Z. Lan, G. Q. Ren, D. G. Chen, F. Huang and M. C. Hong, *J. Am. Chem. Soc.*, 2006, **128**, 12981; (c) W. D. Shi, J. B. Yu, H. S. Wang and H. J. Zhang, *J. Am. Chem. Soc.*, 2006, **128**, 16490.
- (a) X. H. Liu, R. Yi, N. Zhang, R. R. Shi, X. G. Li and G. Z. Qiu, *Chem.-Asian J.*, 2008, **3**, 732; (b) H. P. Cong and S. H. Yu, *Cryst. Growth Des.*, 2009, **9**, 210; (c) M. Li and S. Mann, *Langmuir*, 2000, **16**, 7088.
- (a) M. Ghosh, E. V. Sampathkumaran and C. N. R. Rao, *Chem. Mater.*, 2005, **17**, 2348; (b) L. P. Li, X. F. Sun, X. Q. Qiu, J. X. Xu and G. S. Li, *Inorg. Chem.*, 2008, **47**, 8839; (c) W. S. Seo, J. H. Shim, S. J. Oh, E. K. Lee, N. H. Hur and J. T. Park, *J. Am. Chem. Soc.*, 2005, **127**, 6188.
- (a) K. T. Nam, D. W. Kim, P. J. Yoo, C. Y. Chiang, N. Meethong, P. T. Hammond, Y. M. Chiang and A. M. Belcher, *Science*, 2006, **312**, 885; (b) X. W. Lou, D. Deng, J. Y. Lee and L. A. Archer, *J. Mater. Chem.*, 2008, **18**, 4397.
- T. E. Davies, T. García, B. Solsona and S. H. Taylor, *Chem. Commun.*, 2006, 3417.
- Y. G. Li, B. Tan and Y. Y. Wu, *J. Am. Chem. Soc.*, 2006, **128**, 14258.
- K. An, N. Lee, J. Park, S. C. Kim, Y. Hwang, J. G. Park, J. Y. Kim, J. H. Park, M. J. Han, J. Yu and T. Hyeon, *J. Am. Chem. Soc.*, 2006, **128**, 9753.
- (a) J. Feng and H. C. Zeng, *Chem. Mater.*, 2003, **15**, 2829; (b) R. Xu and H. C. Zeng, *J. Phys. Chem. B*, 2003, **107**, 926.
- (a) R. Qiao, X. L. Zhang, R. Qiu, J. C. Kim and Y. S. Kang, *Chem.-Eur. J.*, 2009, **15**, 1886; (b) G. B. Sun, X. Q. Zhang, M. H. Cao, B. Q. Wei and C. W. Hu, *J. Phys. Chem. C*, 2009, **113**, 6948.
- A. M. Cao, J. S. Hu, H. P. Liang, W. G. Song, L. J. Wan, X. L. He, X. G. Gao and S. H. Xia, *J. Phys. Chem. B*, 2006, **110**, 15858.
- H. Y. Liang, J. M. Raitano, L. H. Zhang and S. W. Chan, *Chem. Commun.*, 2009, 7569.
- D. Barreca, A. Gasparotto, O. I. Lebedev, C. Maccato, A. Pozza, E. Tondello, S. Turner and G. V. Tendeloo, *CrystEngComm*, 2010, **12**, 2185.
- T. Y. Wei, C. H. Chen, K. H. Chang, S. Y. Lu and C. C. Hu, *Chem. Mater.*, 2009, **21**, 3228.
- Y. S. Ding, L. P. Xu, C. H. Chen, X. F. Shen and L. S. Steven, *J. Phys. Chem. C*, 2008, **112**, 8177.
- Y. K. Liu, G. H. Wang, C. K. Xu and W. Z. Wang, *Chem. Commun.*, 2002, 1486.
- (a) H. Tüysüz, Y. Liu, C. Weidenthaler and F. Schüth, *J. Am. Chem. Soc.*, 2008, **130**, 14108; (b) Y. L. Zhang, J. Zhu, X. Song and X. H. Zhong, *J. Phys. Chem. C*, 2008, **112**, 5322; (c) Y. G. Li, B. Tan and Y. Y. Wu, *Nano Lett.*, 2008, **8**, 265; (d) Y. Z. Shao, J. Sun and L. Gao, *J. Phys. Chem. C*, 2009, **113**, 6566; (e) G. X. Wang, X. P. Shen, J. Horvat, B. Wang, H. Liu, D. Wexler and J. Yao, *J. Phys. Chem. C*, 2009, **113**, 4357.
- (a) C. Feldmann, *Adv. Funct. Mater.*, 2003, **13**, 101; (b) X. W. Wei, G. X. Zhu, Y. J. Liu, Y. H. Ni, Y. Song and Z. Xu, *Chem. Mater.*, 2008, **20**, 6248; (c) L. P. Zhu, H. M. Xiao, W. D. Zhang, G. Yang and S. Y. Fu, *Cryst. Growth Des.*, 2008, **8**, 957.
- (a) C. Feldmann and H. O. Jungk, *Angew. Chem., Int. Ed.*, 2001, **40**, 359; (b) D. Caruntu, G. Caruntu, Y. X. Chen and C. O'Connor, *Chem. Mater.*, 2004, **16**, 5527; (c) Z. W. Quan, C. X. Li, X. M. Zhang, J. Yang, P. P. Yang, C. M. Zhang and J. Lin, *Cryst. Growth Des.*, 2008, **8**, 2384; (d) Z. C. Orel, A. Anžlovar, G. Drazžić and M. Zyigon, *Cryst. Growth Des.*, 2007, **7**, 453.
- (a) M. Ocaña, M. P. Morales and C. J. Serna, *J. Colloid Interface Sci.*, 1999, **212**, 317; (b) S. Y. Ho, A. S. W. Wong and G. W. Ho, *Cryst. Growth Des.*, 2009, **9**, 732; (c) L. S. Zhong, J. S. Hu, H. P. Liang, A. M. Cao, W. G. Song and L. J. Wan, *Adv. Mater.*, 2006, **18**, 2426; (d) L. Z. Zhang, J. C. Yu, A. W. Xu, Q. Li, K. W. Kwong and S. H. Yu, *J. Cryst. Growth*, 2004, **266**, 545.
- (a) M. Hirano and H. Morikawa, *Chem. Mater.*, 2003, **15**, 2561; (b) R. Si, Y. W. Zhang, S. J. Li, B. X. Lin and C. H. Yan, *J. Phys. Chem. B*, 2004, **108**, 12481; (c) C. L. Yan and D. F. Xue, *J. Phys. Chem. B*, 2005, **109**, 12358.
- (a) C. Feldmann and C. Metzmacher, *J. Mater. Chem.*, 2001, **11**, 2603; (b) Z. L. Wang, Z. W. Quan, P. Y. Jia, C. K. Lin, Y. Luo, Y. Chen, J. Fang, W. Zhou, C. J. O'Connor and J. Lin, *Chem. Mater.*, 2006, **18**, 2030.
- (a) D. Caruntu, G. Caruntu, Y. X. Chen, C. J. O'Connor, G. Goloverda and V. L. Kolesnichenko, *Chem. Mater.*, 2004, **16**, 5527; (b) J. Yang, C. X. Li, Z. W. Quan, D. Y. Kong, X. M. Zhang, P. P. Yang and J. Lin, *Cryst. Growth Des.*, 2008, **8**, 695.
- (a) H. C. Zeng, *J. Mater. Chem.*, 2006, **16**, 649; (b) F. Cao, W. Hu, L. Zhou, W. D. Shi, S. Y. Song, Y. Q. Lei, S. Wang and H. J. Zhang, *Dalton Trans.*, 2009, 9246; (c) Z. Chen, L. W. Qian, J. Zhu, Y. P. Yuan and X. F. Qian, *CrystEngComm*, 2010, **12**, 2100.
- (a) K. Rida, A. Benabbas, F. Bouremmad, M. A. Pen, E. Sastre and A. artinez-Arias, *Appl. Catal., A*, 2007, **327**, 173; (b) M. Gharagozlou, *J. Alloys Compd.*, 2009, **486**, 660.
- (a) L. H. Hu, Q. Peng and Y. D. Li, *J. Am. Chem. Soc.*, 2008, **130**, 16136; (b) L. P. Zhou, J. Xu, H. Miao, F. Wang and X. Q. Li, *Appl. Catal., A*, 2005, **292**, 223; (c) T. E. Davies, T. García, B. Solsona and S. H. Taylor, *Chem. Commun.*, 2006, 3417.
- (a) G. Binotto, D. Larcher, A. S. Prakash, R. H. Urbina, M. S. Hegde and J. M. Tarascon, *Chem. Mater.*, 2007, **19**, 3032; (b) S. L. Xiong, C. Z. Yuan, X. G. Zhang, B. J. Xi and Y. T. Qian, *Chem.-Eur. J.*, 2009, **15**, 5320; (c) X. W. Lou, D. Deng, J. Yang and L. L. A. Archer, *J. Mater. Chem.*, 2008, **18**, 4397.
- (a) V. Kesavan, P. S. Sivanand, S. Chandrasekaran, Y. Koltypin and A. Gedanken, *Angew. Chem., Int. Ed.*, 1999, **38**, 3521; (b) N. Perkass, Y. Koltypin, O. Palchik, A. Gedanken and S. Chandrasekaran, *Appl. Catal., A*, 2001, **209**, 125; (c) L. P. Zhou, J. Xu, C. Chen, F. Wang and X. Q. Li, *J. Porous Mater.*, 2006, **15**, 7.
- (a) H. G. Yu, J. G. Yu, S. W. Liu and S. Mann, *Chem. Mater.*, 2007, **19**, 4327; (b) T. Masui, Y. M. Peng, K. I. Machida and G. Y. Adachi, *Chem. Mater.*, 1998, **10**, 4005; (c) H. M. Chen, R. S. Liu, M. Y. Lo, S. C. Chang, L. D. Tsai, Y. M. Peng and J. F. Lee, *J. Phys. Chem. C*, 2008, **112**, 7522.
- (a) R. M. Wang, C. M. Liu, H. Z. Zhang, C. P. Chen, L. Guo, H. B. Xu and S. H. Yang, *Appl. Phys. Lett.*, 2004, **85**, 2080; (b) E. L. Salabas, A. Ruplecker, F. Kleitz, F. Radu and F. Schüth, *Nano Lett.*, 2006, **6**, 2977.
- (a) C. Nethravathi, S. Sen, N. Ravishankar, Rajamathi, C. Pietzonka and B. Harbrecht, *J. Phys. Chem. B*, 2005, **109**, 11468; (b) Z. Dong, Y. Y. Fu, Q. Han, Y. Y. Xu and H. Zhang, *J. Phys. Chem. C*, 2007, **111**, 18475.